HIGH-STRAIN RATE SPALL STRENGTH MEASUREMENT OF A CO-CR-FE-MN-NI HIGH-ENTROPY ALLOY

by

Andrew Ehler

A Thesis

Submitted to the Faculty of Purdue University

In Partial Fulfillment of the Requirements for the degree of

Master of Science in Aeronautics and Astronautics

School of Aeronautics & Astronautics

West Lafayette, Indiana

December 2022

THE PURDUE UNIVERSITY GRADUATE SCHOOL
STATEMENT OF COMMITTEE APPROVAL

Dr. Vikas Tomar, Chair

School of Aeronautics and Astronautics

Dr. Tyler Tallman

School of Aeronautics and Astronautics

Dr. Dianyun Zhang

School of Aeronautics and Astronautics

Approved by:

Dr. Gregory A. Blaisdell

Dedicated to my mother who told me to 'Suck it up'…
but showed me how to keep on fighting as well

ACKNOWLEDGMENTS

I would like to acknowledge Sandia National Labs for their financial support of this research. I would also like to acknowledge the Purdue Military Research Initiative, Col (ret) Dave Hankins, and Dr. Eric Dietz for their support in providing this research opportunity. Finally, I would like to acknowledge my advisor, Dr. Vikas Tomar, and my friends and colleagues in the Interfacial Multiphysics Lab group for their continuous help and guidance.

TABLE OF CONTENTS

LIST OF FIGURES

LIST OF ABBREVIATIONS

AM – Additively Manufactured

DED – Directed-Energy Deposition

DPS – Doppler Pin System

EDS – Energy Dispersive Spectroscopy

EOS – Equation of State

HEA – High-Entropy Alloy

HEL – Hugoniot Elastic Limit

LENS – Laser-Engineered Net Shaping

LIPIT – Laser-Induced Projectile Impact Testing

LIF – Lithium Fluoride

MD – Molecular Dynamics

PDV – Photon Doppler Velocimetry

PMMA – Polymethyl Methacrylate

SEM – Scanning Electron Microscope

VISAR – Velocity Interferometer System for Any Reflector

LIST OF SYMBOLS

ρ – Material Density

U_P – Particle Velocity

U_S – Shock Velocity

V – Impact Velocity

c_0 – Bulk Sound Speed

s – Hugoniot Coefficient

$\dot{\varepsilon}$ – Strain Rate

Δv – Velocity Pullback

Δt – Pullback Duration

ABSTRACT

This work explored the dynamic behavior and failure mechanisms of an additively manufactured high-entropy alloy (HEA) when subjected to high-strain rate shock impacts. A laser-induced projectile impact testing (LIPIT) setup was used to study the dynamic behavior of the Cantor alloy CoCrFeMnNi samples manufactured using a directed-energy deposition technique. HEA flyers were accelerated by a pulse laser to velocities up to 1 km/s prior to impact with lithium fluoride glass windows. A photon Doppler velocimetry (PDV) system recorded the velocity of the flyer during the acceleration and subsequent impact. From this velocity profile, the Hugoniot coefficient and sound speed of the HEA samples were determined.

Upon determination of key shock parameters, spallation occurring due to shock was analyzed. Using the same LIPIT and PDV systems as the earlier testing, aluminum flyers of various thicknesses were accelerated into HEA samples. The back-surface velocity profiles of the HEA samples showed a characteristic "pullback" caused by the interaction of the tensile stress waves indicative of spall occurrence in the material. The magnitude of this pullback and the material properties determined in the first experiments allow for the measurement of spall strength at various strain-rates. This data is compared to previous data looking at similar HEAs manufactured using traditional methods. A comparison of this data showed that the spall strength of the HEA samples was equivalent to that of similar alloys but at significantly higher strain rates. As an increased strain-rate tends to result in increased spall strengths, further examination was needed to determine the reasons for this decreased spall strength in the AM samples.

Post-shock specimen recovery allowed for the failure mechanisms behind the spallation to be observed. Scanning electron microscope (SEM) images of the cross-section of the samples showed ductile fracture and void growth outside of the predicted spall region. Further imaging using energy dispersive spectroscopy (EDS) showed the presence of potentially chromium-oxide deposits in regions outside of the predicted spall plane. It is hypothesized that these regions created nucleation points about which spallation occurred. Thus, to achieve spall strength in AM HEAs equivalent to strengths in traditionally-casted alloys, the AM sample must be refined to reduce the occurrence of these deposits and voids.

1. INTRODUCTION

High-entropy alloys (HEA) are a class of relatively novel materials that possess certain advantageous characteristics when compared to conventional alloys. The unique compositions of these materials make them more beneficial under certain loading conditions and environments than previous alloys. A particular HEA, the Cantor alloy CoCrFeMnNi, has shown strong potential for use in a variety of intense environmental conditions, particularly within the field of aerospace. While this HEA was one of the earliest to be produced and experimentally studied, recent developments in additive manufacturing techniques present new avenues for cheaper, faster, and more adaptable production processes of materials key to the ever-evolving aerospace domain.

However, the nature and implications of these new processes on the composition and microstructure of these materials are not fully understood. This work seeks to address these shortcomings by quantifying the difference in high-strain rate loading behaviors between an additively manufactured HEA and its traditionally casted counterparts. By then identifying the underlying microstructural differences responsible for these differences, refinement of the additive manufacturing process can thus seek to eliminate these differences. This is critical in ensuring these materials can withstand the pressing conditions they will be subjected to during use.

Evaluating the behavior of a material under extreme dynamic loading conditions can require costly and complex experimental setups. While these setups have proved useful, they have become unable to fully support the increasing demand in testing for a wide range of new materials being produced each year. Thus, there is a need for a more efficient, cost-effective way to address this growing problem. In Chapter 3 of this work, a method to evaluate the dynamic behavior of the CoCrFeMnNi HEA during high-strain rate loading conditions is discussed. This system uses a high-energy pulse laser to accelerate a flyer to velocities of more than 1 km/s. Another laser system uses photon Doppler velocimetry (PDV) to determine the velocities of exposed surfaces present during testing. These velocity profiles allow for key dynamic parameters and characteristics of the HEA to be determined. This system is thus both significantly cheaper and accessible than other competing experimental setups while still producing reliable, valuable data.

The latter half of Chapter 3 will quantify and discuss the differences observed in the performance of an additively manufactured CoCrFeMnNi sample compared to previous experimental studies on traditionally-cast specimens. The microstructural features of the tested

specimens are then explored. Conclusions are drawn regarding the implications of these features on the behavior of the specimens and steps which can mitigate the effects of these differences in the future.

2. LITERATURE BACKGROUND

The production and use of alloys extends to ancient times when early civilizations realized the benefits of combining multiple elements to create a single compound. [1] However, within the last several decades, significant work has focused on creating a new type of metallurgical alloy, a high-entropy alloy (HEA). While most conventional alloys are composed primarily of one or two components with lesser quantities of other supplemental elements, HEAs are composed of four or more components in equiatomic or near-equiatomic proportions. [2] The first of these HEAs to be successfully produced, and the HEA of primary focus in this study, is known as the Cantor alloy, CoCrFeMnNi. [3]

HEAs are advantageous because of the mechanical properties they possess owing to their unique metallic structures. The CoCrFeMnNi HEA is a single-phase FCC-structure that initially proved to be highly damage tolerant due to its high strength, high fracture toughness, and ductility. [4] Further research into this HEA showed that these material properties improved as temperature decreased. Nano-twinning of the crystal boundaries was observed at cryogenic temperatures resulting in strain-hardening that is not possible with other conventional alloys. [5] Introducing the material into a low-temperature environment increases its fracture toughness and strength which is not found in other cryogenic alloys such as cryogenic steels. A high fracture-resistant, high-energy absorbing, high strength-to-weight material that can maintain these properties across a large temperature range such as the Cantor alloy becomes an attractive candidate for the aerospace domain. Incorporating this technology into use, however, requires a better understanding of the manufacturing process behind these materials.

HEAs are known as high-entropy because of the large increase in mixing entropy required to create a metallic microstructure of multiple components in large proportions. [2] This makes their production exceedingly complex compared to traditional alloys. The original method used to synthesize this material involved mixing ingots of pure metals within a pure argon atmosphere. [3, 6] This mixture is remelted several times to improve chemical homogeneity before being placed into a mold to solidify. [6] While this has become a reliable method to create consistent Cantor specimens, there are limitations in this production process common among mold-casting techniques including increased cost and geometry limitations. [7]

Additive manufacturing is often turned to as a solution to address these problems. A variety of AM methods have been developed in order to print metallic materials with many of these being extended towards the development of AM HEAs [8], including the CoCrFeMnNi HEA. These processes are often based on powder bed techniques such as powder-bed fusion [9] or slight variations thereof in the case of selective laser melting [10]. To produce the AM materials, pure powders of the elemental components are mixed in their proper proportions. These are then placed on the bed or build plate in thin layers. A high-energy source such as a laser or electron beam fuses these powders to form the HEA with microstructural features like those of a cast HEA.

A competing set of AM methods to produce HEAs are found in directed energy deposition (DED) techniques. In slight contrast to powder-bed based techniques, the metal powder is applied simultaneously to the melting of the surface by a laser. [8] The powder is injected into the system as the build plate or laser transverses. This allows for faster and larger builds than powder-bed based techniques. The CoCrFeMnNi samples used in this work were produced using a particular DED technique, laser engineered net shaping (LENS). In this method, the powder is fed toward the focal point of a beam where it is then melted. The laser-powder system remains stationary while the build plate is translated to allow for rapid solidification of the material. Additional layers can then be added to create a near net-shape bulk structure. [11]

Initial trials to additively manufacture CoCrFeMnNi using this method proved successful. [12] As-built samples directly from the prints showed high yield strength and ductile fracture, but they did not possess the same strain-hardening rates that are otherwise present in their cast counterparts. An annealing process applied to the as-built prints formed twin boundaries in the microstructure resulting in mechanical properties equivalent to those of cast specimens. These annealed AM specimens were thus much improved from previous attempts to AM the CoCrNiFeMn HEA in replicating these features. However, there were some notable microstructural differences between the cast specimens and the AM specimens. Oxide deposits were observed randomly throughout the material which disrupted the grain boundaries. During tensile tests, aluminum-oxide deposits – despite Al being only found in trace amounts throughout the material – acted as initiation points from which voids formed. It could not be concluded whether seeking to fully eliminate these Al-oxide deposits would eliminate these dimple formations or if other oxide deposits containing Cr- or Mn- would cause similar behaviors.

Another key evaluation criterion to compare the AM HEA specimen to its as-cast specimen counterparts is its response under high-strain rate loading conditions. The ability of these materials to resist fracture when subjected to high-speed impacts makes them highly desirable for the aerospace domain. Being able to leverage the advantages of AM while maintaining the original characteristics of the Cantor alloy is necessary for future implementation of this material. Thus, it is important to ensure these properties are retained in the AM specimens.

During high-velocity impacts, shock waves form in the material. These shock waves propagate in both directions from the impact location – back into the impactor itself and forward into the impacted material. In most cases, the propagation of these shock waves is governed according to Hugoniot equations of state (EOS) for each of the materials. These EOS allow for the shock wave velocity to be related to the particle velocity behind it. [13] Upon initial impact, compressive shock waves propagate in both directions through the thickness of the materials. Whenever these waves reach a free surface or another low-impedance feature in the material, they reflect and become tensile waves. When tensile waves interact with each other, they create large tensile stresses in the material. The large stresses under dynamic shock conditions allow for the rapid nucleation of microcracks and the growth of voids. [14] These fractures and defects often result in fragmentation of the material referred to as spall.

Spall fracture in material occurs at several thresholds of damage beginning at incipient fracture to an intermediate stage before progressing to the main crack formation. The rate of damage progression between these stages is dependent on the decompression rate of the free surface upon reflection of the initial shock wave. Shock waves traveling at greater velocities result in greater decompression rates on the free surface. Therefore, high-velocity initial shock waves will slow the overall fracture process allowing the material to better resist spallation. The shock wave speed and corresponding decompression rate relate to the strain rate induced by the impactor. Thus, most materials demonstrate a strain-rate dependence between this decompression rate and the ability of the material to resist spall fracture, or its spall strength.

Measuring the spall strength of the material allows for the quantification of its performance to resist spallation. The spall strength of the material is the maximum tensile stress attained during a spall fracture. Several different methods have been used over time to study and measure this phenomenon. At a fundamental level, spall strength experiments rely on an impactor traveling at high velocities to create a shock event within the target material. Accelerating the impactor to great

enough velocities to generate spall fracture is often done through either the use of lasers, gas-guns, or explosives. As the wave travels towards and reflects off the free surface of the target, the free surface begins to travel at the particle velocity behind the shock wave. This surface begins to return to rest as the wave leaves until accelerating again when the wave returns once again after its tensile interaction. A velocity interferometer system for any reflector (VISAR) is traditionally used to record this velocity profile and the change in velocity is observed between the initial arrival of the shock wave and its return reflection. This change in velocity and the EOS properties for shock in the material determine the spall strength of the material.

These velocity profiles reveal details of spall fracture behaviors in a material including the rate of the fracture process and the degree of completion for the spall damage. However, these profiles are unable to provide full descriptions of the failure mechanisms present. Post-shock analyses of experimentally tested specimens are necessary for these qualitative assessments. Brittle materials show signs of cracking at failure locations whereas ductile fracture results in the nucleation and growth of voids in the material. In the case of the CoCrFeMnNi HEA, post-spall fracture studies on cast specimens revealed significant plastic deformation in the forms of dislocations and the formation of twin boundaries. [15] At higher-strain rates, the presence of these twin boundaries increased due to strain hardening confirming a strain-rate dependence for spall strength.

While measurements of spall strength and analyses of spall fracture have been studied for nearly 60 years and can be conducted on most pulsed laser systems, these calculations rely on the EOS parameters to already be known. The systems for determining these have tended to be much more complex than those used to determine spall strength. The Hugoniot coefficients for the EOS are found through an impedance-mismatch technique utilizing conservations of mass, momentum, and energy to equate the impact, particle, and shock velocities in the flyer to the shock and particle velocities in the target. [13] Furthermore, an elastic component in the energy balance known as the Hugoniot elastic limit (HEL) describes the maximum compressive stress the material can withstand prior to plastic deformation. [16] The traditional spall strength experimental setups which only measure the back surface velocity of the target are not capable of measuring these data points.

In order to measure the requisite data points for the determination of these values, a gas-gun experimental setup using an electric pin technique is commonly used to measure the shock wave

speed. [17] Electric pins are placed on the front and back surfaces of the target. The velocity profile of the impactor is still read using a VISAR or similar system and, upon impact, the pins determine the time for the shock wave to travel across the thickness to determine wave speed. Gas-gun systems are expensive and difficult to access. Additionally, the size of the flyers required to install the necessary pin systems can be several millimeters in thickness or more. This makes most pulsed lasers unable to accelerate them to sufficient speeds required to induce shock wave propagations.

Methods have been proposed to make a determination of the EOS parameters less prohibitive. Previous studies have shown that there is the potential to use pulsed laser setups like those used for spall strength measurements to make EOS determinations. [18-19] In these setups, the material of interest is used as the impactor while a transparent material that allows for velocity determinations is chosen as the target. This allows for the front surface of the impactor to be recorded throughout a test providing both the impact and particle velocities immediately after impact. By selecting a known target material with a linear Hugoniot EOS [20] in the velocity range of interest, it is possible to determine the shock parameters of the desired material. This technique has one significant disadvantage. While the target is often a glass with an insignificant HEL, the HEL of the flyer is unable to be determined from the velocity profile of the front surface of the impactor. Instead, approximations of this value are made utilizing data from similar materials.

Accessibility of requisite systems can be increased through the adaption of the velocimetry measurement systems. While VISAR has often been used and is relatively inexpensive and compact, abrupt velocity changes and surface changes during testing make it sometimes unreliable. [21] An alternate system has been purposed in the way of Photon Doppler Velocimetry (PDV). [22] These systems utilize continuous wave fiber lasers and fiber optic components to create a Doppler shift in the laser beam caused by a moving surface. The shifted beam is compared to the original signal to determine the magnitude of the frequency shift over time. These frequencies in the time domain are then related to velocity according to the wavelength. This system is both less expensive than VISAR systems and capable of extracting weak signals from testing that would otherwise be lost.

The traditional PDV system described above is homodyne because of its use of the same signal at both the surface interface and the mixed signal. As a result, a noise band is often created at frequencies less than 100 MHz. Therefore, low-velocity profiles are often indistinguishable from this noise. To counter this issue, heterodyne PDV systems have been proposed. [23] These systems

implement an additional continuous wave laser operating at a slightly higher wavelength to replace the original signal from being mixed with the Doppler-shifted signal. This upshifts the noise band away from the testing velocity range. Lower velocity profiles can then be measured. Material behaviors at these low velocities can prove important in determining the Hugoniot EOS.

The development of HEAs has presented many opportunities for their applications to aerospace technologies. In particular, the CoCrFeMnNi HEA has shown promise for cryogenic applications due to its high fracture toughness and strength. The ability to AM this material is vital as we look to realize the potential of this material for real-world applications. Much is still unknown regarding the implications of these AM processes on the microstructure and dynamic behavior of the Cantor HEA. The continued development of this technology, therefore, rests on the ability to measure these performances in a way that is both accurate and accessible. In the following chapter, an experimental setup incorporating the concepts discussed here is proposed to address this need.

3. ARTICLE: HIGH-STRAIN RATE SPALL STRENGTH MEASUREMENT FOR COCRFEMNNI HIGH-ENTROPY ALLOY

This article has been published in *Metals* under DOI: https://doi.org/10.3390/met12091482

Andrew Ehler[1], Abhijeet Dhiman[1], Tyler Dillard[1], Remi Dingreville[2], Erin Barrick[3], Andrew Kustas[4], and Vikas Tomar[1]

[1] School of Aeronautics and Astronautics, Purdue University, West Lafayette, IN 47907, USA; aehler@purdue.edu (A.E.); adhiman@purdue.edu (A.D.); tdillard@purdue.edu (T.D.); tomar@purdue.edu (V.T.)
[2] Center for Integrated Nanotechnologies, Sandia National Laboratories, Albuquerque, NM 87185, USA; rdingre@sandia.gov
[3] Metallurgy and Materials Joining Department, Sandia National Laboratories, Albuquerque, NM 87185, USA; ejbarri@sandia.gov
[4] Coatings and Additive Manufacturing Department, Sandia National Laboratories, Albuquerque, NM 87185, USA; akustas@sandia.gov

3.1 Abstract

In this study, we experimentally investigate the high stain rate and spall behavior of Cantor high-entropy alloy (HEA), CoCrFeMnNi. First, the Hugoniot equations of state (EOS) for the samples are determined using laser driven CoCrFeMnNi flyers launched into known Lithium Fluoride (LiF) windows. Photon Doppler Velocimetry (PDV) recordings of the velocity profiles find the EOS coefficients using an impedance mismatch technique. Following this set of measurements, laser-driven aluminum flyer plates are accelerated to velocities of 0.5–1.0 km/s using a high-energy pulse laser. Upon impact with CoCrFeMnNi samples, the shock response is found through PDV measurements of the free surface velocities. From this second set of measurements, the spall strength of the alloy is found for pressures up to 5 GPa and strain rates in excess of 10^6 s^{-1}. Further analysis of the failure mechanisms behind the spallation is conducted using fractography revealing the occurrence of ductile fracture at voids presumed to be caused by chromium oxide deposits created during the manufacturing process.

Keywords: high-entropy alloy; cantor alloy; equation of state; spall strength; laser-induced projectile impact testing; Photon Doppler Velocimetry

3.2 Introduction

High-entropy alloys (HEAs), particularly those composed of at least four elemental constituents with equimolar or near-equimolar components, have shown great promise for applications in aviation and aerospace fields owing to their high strength and thermal stability at high temperatures [1–3]. The so-called Cantor alloy, equiatomic CoCrFeMnNi, has been of particular interest. This specific quinary HEA possesses a combination of high strength and high ductility [4–9], as well as the ability to sustain high levels of fracture toughness at extremely low temperatures [7–9]. These properties make CoCrFeMnNi a strong candidate as a structural material for a range of applications for which high strength and fracture resiliency are key, particularly in aerospace and nuclear applications. However, continued research is needed to fully understand how these materials perform under dynamic-loading conditions. More specifically, the shock properties of HEAs at ultra-high strain rates are of significant interest to the fundamental shock physics community and to the broader scientific community.

Previous investigations into the spall strength and equations of state (EOS) of conventional structural materials involve the use of single-stage gas guns in combination with a variety of measurement methods such as a Doppler Pin System (DPS) [10] or Photo Doppler Velocimetry (PDV) [11] to record free surface velocities in order to derive spall strength and EOS. For instance, Jiang et al. [12] used a gas-gun system setup to investigate the dynamic response of CoCrFeMnNi alloys, including the Hugoniot elastic limit (HEL) and EOS coefficients. Gas-gun systems, however, are not always readily available to provide an abundant amount of high-throughput data across a broad range of impact velocities. As an alternative, recent research has been trending towards using high-energy single-pulse lasers to achieve high-velocity impacts in order to investigate spall strengths and failure mechanisms for various materials [13–18].

Lou et al. [19] and Swift et al. [20] developed a laser-launch system capable of determining EOS using Cu, Ga, and NiTi flyers impacting a known polymethyl methacrylate, PMMA, target with flyer impact velocities less than 200 m/s. Further studies demonstrated that combining several high-energy lasers can extend the velocity range for impacts in these studies in excess of 10 km/s [21]. The extension of this system to high-energy single-pulse lasers used to investigate spall strength to determine materials' EOS is a viable and efficient technique as it allows for a decreased timeline of the evaluation of a variety of emerging materials with respect to their responses under shock loading conditions.

In addition to the experimental studies, previous research has also shown that the behavior of HEAs under high-strain rate loading conditions can be assessed through numerical simulations. Molecular dynamics (MD) simulations have been used to further analyze the spall strength and failure mechanisms [22,23]. These simulations have been used to numerically predict spall strengths of materials and their relations to strain rates as well as determine the failure mechanisms at the atomic scale. However, successful modeling of these physics has sometimes relied upon the experimental results for EOS [23]. Furthermore, experimental results serve as a useful determination in assessing the accuracy of these models. Thus, reliable experimental findings are required prior to the full implementation of numerical analyses.

In this article, we report the design and results of experiments conducted to obtain the equation of state (EOS) and spall strength of an additively manufactured CoCrFeMnNi HEA at high strain rate for the first time. Specifically, we conducted high-strain rate experiments ($>10^6\ s^{-1}$) that rely on high-speed impact loading to generate large dynamic hydrostatic stresses in a target material. A laser-induced projectile impact testing (LIPIT) setup allows for the acceleration of thin metal flyers at velocities more than ~1 km/s. PDV measurements record velocity profiles during the impacts in order to derive the key parameters to describe the dynamic behavior of the Cantor samples. Post-shock specimen recovery allows for simple analysis of void nucleation and fragmentation due to spalling of CoCrFeMnNi HEA. This study provides further insight into the microstructural features of the additively manufactured specimens that can act as failure mechanism sites within this material.

3.3 Materials and Methods

In this study, we investigated shock properties of an additively manufactured CoCrFeMnNi HEA sample using a laser-based flyer plates system with micron-scale disk impactors. The HEA samples were manufactured using a laser-based directed energy deposition (DED) technique, Laser Engineered Net Shaping (LENS) [24]. The samples provided for testing were rectangular with an original thickness of approximately 300 μm and are shown in Figure 2.1. To create the disk impactors required for testing, these samples were then polished using increasingly fine-grit sandpaper to reduce the specimen to the desired thickness while maintaining planarity along the surface in order to ensure consistent impact velocities and profiles. Additionally, the polishing process resulted in a mirrored finish along the surface, increasing the flyers' reflectivity. This

mirrored finish was intended to maximize the reliability of photon Doppler velocimetry (PDV) measurements. Finally, 1.5 mm diameter flyers were punched from these prepared specimens for testing. Punching of the disks was reserved for the final step to avoid creating irregularities of the both the surface and overall shape of the flyers.

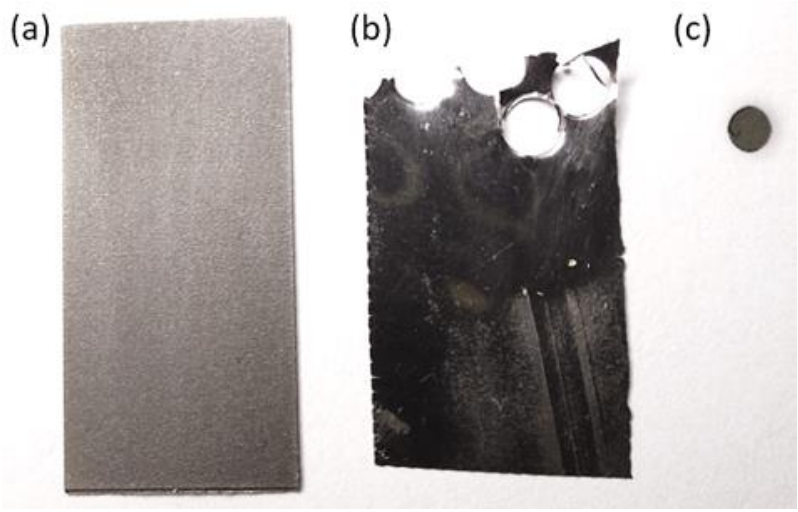

Figure 3.1. (a) Additively manufactured specimen (b) Polished specimen (c) Punched flyer cut-out from (b).

The testing equipment utilized in these studies is a modified version of the micron-scale impact platform developed and used in previous studies [25,26]. The laser-based impact setup used is shown in Figure 2.2, where the flyer is a thin foil launched by intense laser pulses, accelerating up to ~1 km/s in less than 100 ns. The flyer launch assembly consists of CoCrFeMnNi HEA impactors of 10–25 μm thickness glued to glass substrates. A high-energy nanosecond pulsed laser delivered a spatially homogeneous convergent beam directed through the glass to the glass–epoxy–flyer interface. An Nd:YAG laser, Continuum laser, was used, that produces up to 0.75 J at 1.064 μm, with a nominal pulse duration of 8 ns. A uniform beam profile was generated using a 25 mm diameter diffractive optical element (HOLO/OR). After the diffractive optic, the beam was focused with an aspheric objective lens with a 60 mm focal length to produce an 800 μm homogenized focused spot concentric with the flyer disk.

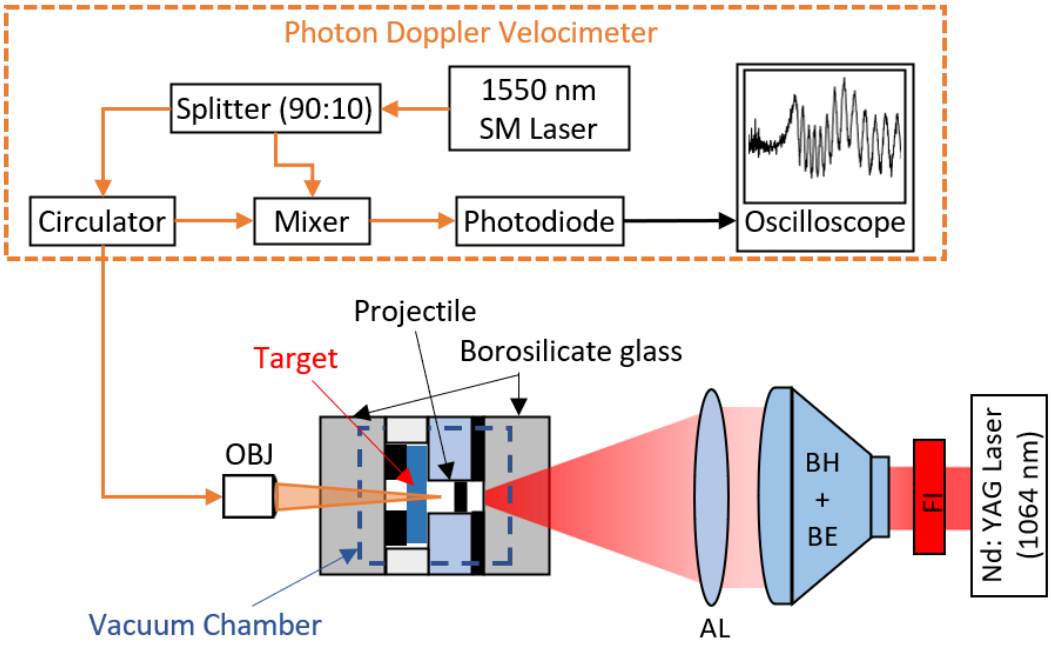

Figure 3.2. Schematic of laser flyer launch system with photon Doppler velocimeter (PDV). BE = beam expander, BH = beam homogenizer, OBJ = objective lens, AL = aspheric lens, FI = Faraday isolator, Reprinted with permission from ref. [25]. Copyright 2022 Springer.

The HEA flyer disk is accelerated inside a vacuum channel of 150 μm length and ultimately impacts a Lithium Fluoride (LiF) glass target with known shock properties [27]. The PDV system depicted in Figure 2.2 uses a single-mode fiber that was collimated to 1.5 mm diameter using a collimator and focused onto the target using an aspheric lens with a long working distance of 17.5 mm. The reflected signal from the flyer was probed through the LiF glass target and mixed with the original reference signal coming from a splitter to create interference. The mixed signal was detected through a 20 GHz photodiode detector and recorded on an oscilloscope. The interferogram produced during the impact was analyzed using a short-term Fourier transform to obtain the impact velocity of the flyer and particle velocity of the target at the flyer–target interface. Since the LiF glass window is a standard material with known EOS, the shock state of the impactor can be deduced via the impedance mismatch technique in Equation (1) [28], where U_S and U_P are the shock and particle velocities found through Equation (2) and Equation (3) respectively.

$$\rho U_{S,HEA} U_{P,HEA} + HEL_{HEA} = \rho U_{S,LiF} U_{P,LiF} + HEL_{LiF} \quad (1)$$

where

$$U_S = c_0 + sU_P \tag{2}$$

and

$$U_{P,HEA} = V - U_{P,LIF} \tag{3}$$

This technique utilizes conservation of mass, energy, and momentum to derive relations between shock and particle velocity between the two mediums. PDV measurements record both the impact velocity, *V*, of the flyer and the particle velocity in the LiF target. These values allow for the Hugoniot pressure to develop in the LiF. Thus, the only remaining unknown in Equation (1) is $U_{S,HEA}$. This system of equations allows for the Hugoniot coefficient *s* and bulk sound speed c_0 to be determined.

Using the same system, slight modifications to the setup were made to investigate the spall strength of the material. Spall strength can be used to provide further insights into the failure and deformation mechanisms of the HEA when the tensile load exceeds the fracture energy and voids nucleate in the material. To perform spall testing of HEA specimens, an aluminum 1100 foil disk was used as an impactor and an HEA foil was used as the target. Figure 2.3a shows the schematic of spall failure inside the HEA target. As shown in this figure, the intersection of reflected shock wave by the free surface of impactor and specimen leads to dynamic tensile stresses that ultimately result in failure. The PDV measurements of velocity along the free surface of the target are used to find the spall strength. We estimate the spall strength by determining the difference between the maximum particle velocity and the minimum of the spall pullback, as depicted by Δv in the free surface velocity profile in Figure 2.3b. The momentum conservation condition in Equation (4) is then applied to estimate spall strength as a function of material properties and this pullback velocity [29], where c_B is the bulk sound speed of the material. The strain rate induced by this impact is calculated according to Equations (4) and (5) [19], such that,

$$\sigma_{spall} = \frac{1}{2}\rho_o c_B \Delta v \tag{4}$$

$$\dot{\varepsilon} \approx \frac{1}{c_B}\frac{du_P}{dt} \approx \frac{1}{2c_B}\frac{\Delta v}{\Delta t} \tag{5}$$

(a)

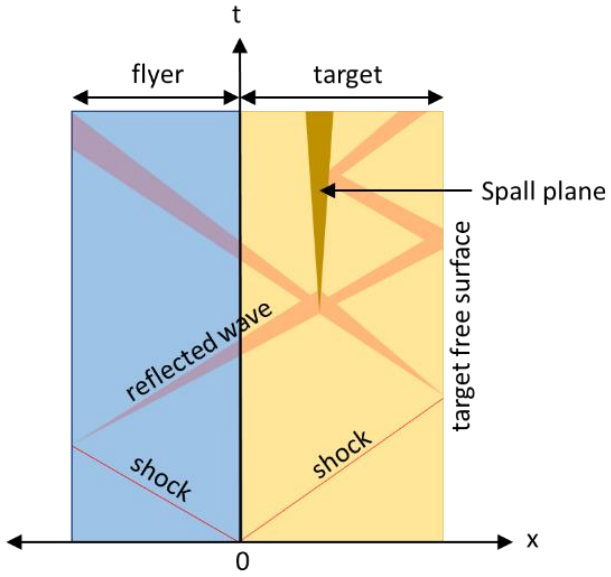

(b)

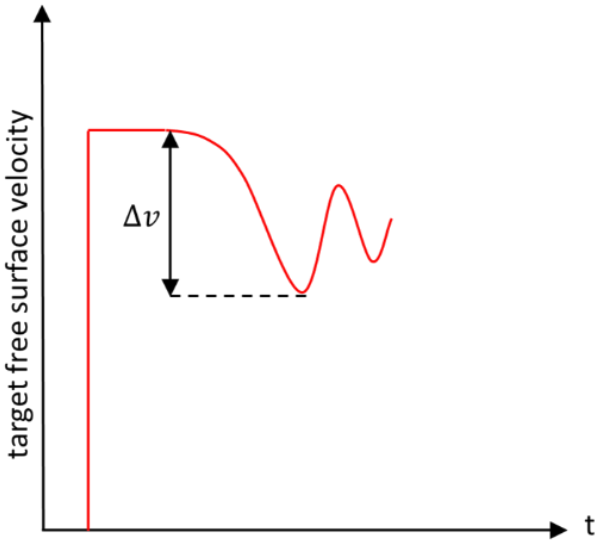

Figure 3.3. (a) Schematic of spall due to flyer impact in Lagrange frame (b) Velocity profile at the free surface of the target during spall failure.

Post-shock specimen recovery reveals further details into the mechanisms present during spallation of the tested specimens. Post-impact optical microscopy image analysis of the HEA target specimen is utilized to evaluate whether there is void nucleation present in the material. In the asymmetric collision between the aluminum flyer and HEA target, there is a change of flyer

speed before and after the collision. High magnification images of the HEA target after impact can be processed to locate the clusters of voids, which can be classified as clusters when linked and in close enough proximity. The density of the voids in the HEA as a function of the calculated shock pressure gives a second measurement for spall strength which can be used to validate the first. Furthermore, scanning electron microscope (SEM) imaging with energy dispersive spectroscopy (EDS) allows for the determination of the microstructural features of the specimens. These features can be linked to failures within the samples in order to ascertain the impacts of AM LENS processes on the dynamic behaviors of the CoCrFeMnNi samples.

3.4 Results and Discussion

3.4.1 Equation of State

Figure 4a shows a velocity history obtained by PDV of the impact faces of an HEA flyer of 25μm thicknesses, launched across a 150 μm gap at LiF glass targets. A laser energy of 800 mJ was used to accelerate the HEA flyers to a velocity of approximately 400 m/s. We note that there is then a sudden reduction in the recorded velocity of the flyer as it impacts the LiF glass target. Figure 4b shows the impact velocity profile around this region. Rather than a sudden decrease in the velocity of the flyer to rest, we measured a period of around 15 ns in which the flyer and LiF glass interface have a relatively constant velocity, as indicated in Figure 4b. This is an indication of the particle velocity within the LiF glass target behind the shock wave induced by the impact of the HEA flyer.

(a)

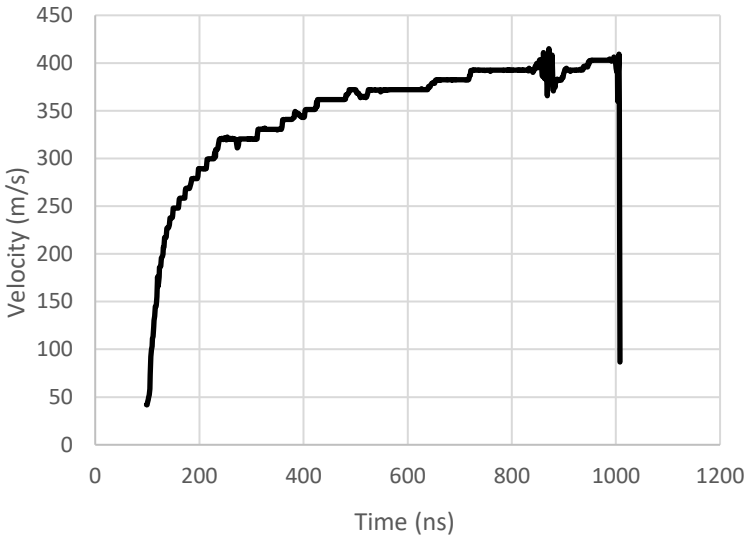

(b)

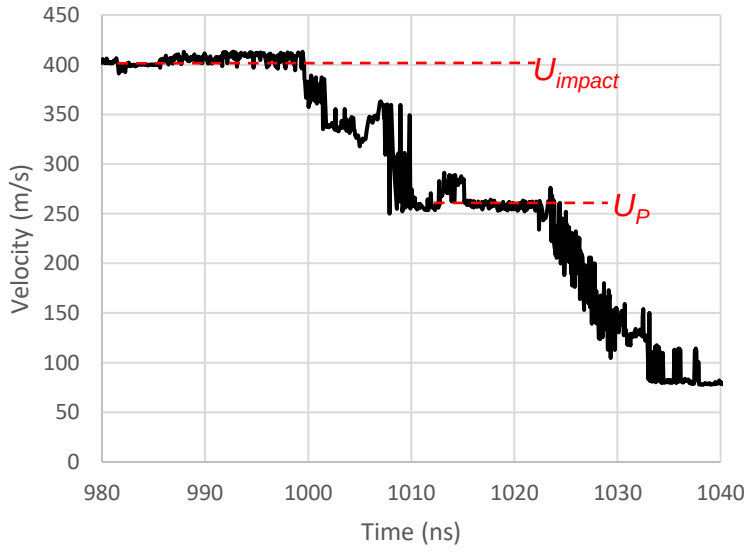

Figure 3.4. (a) Velocity profile of flyer impact on glass (b) Velocity profile measured at the flyer–glass interface.

Using these PDV measurements, we wish to extract two parameters for the flyer/target impacts. These are (i) the flyer impact velocity in free space and (ii) the velocity of the flyer/target interface, or U_{impact} and U_p in Figure 4b, respectively. From the known EOS for the LiF glass target, the relation between shock velocity (U_s) and particle velocity (U_p) for the HEA flyer can be obtained from impedance balance using the U_{impact} and U_p data points. This experiment is then repeated several times with variations in the thickness of the flyer ranging from 10 to 25 μm, allowing for several different impact velocities to be reached. These varying impact velocities

result in unique measured particle velocities in the LiF glass target and thus different U_s–U_p relations are found in the HEA sample.

Plotting each of these relations in Figure 2.5, we observe a general positive relation between particle velocity and shock, as should be expected. Furthermore, these results are compared to those obtained previously using a gas-gun experiment with a DPS [12], which examined drop-cast Cantor alloy, as well as to results of atomistic simulations, which look at the micro-scale relations between the particles to derive Hugoniot pressures. From these results, a linear curve fitting of the U_S–U_P relations allows the Hugoniot coefficients for the CoCrFeMnNi samples examined to be determined. As shown in Figure 2.5, the expected bulk sound speed, *c*, is expected to be 3.97 km/s, with a slope of 2.25 representing the Hugoniot coefficient with a coefficient of determination of 0.10. The Hugoniot coefficient and bulk sound speed reported by Jiang et al. [12] were 1.39 and 4.50 km/s, respectively. A linear approximation of the MD simulation in the same velocity range as these experiments found these values to be 2.92 and 3.48 km/s, respectively.

Our measurements agree with both the findings of the MD simulations and EOS for the same alloy fabricated through a non-AM process determined through use of the gas-gun. However, we point out that these results have more variability than those produced in the gas-gun experiments. The results of this study allow us to compare the AM HEA samples to previous EOS and spall studies of similar materials. Furthermore, the experimental techniques used in this study can be compared to previous techniques, primarily those used in determination of EOS. While there are certain advantages offered by the techniques utilized in the study, there are also deficiencies which must be properly considered.

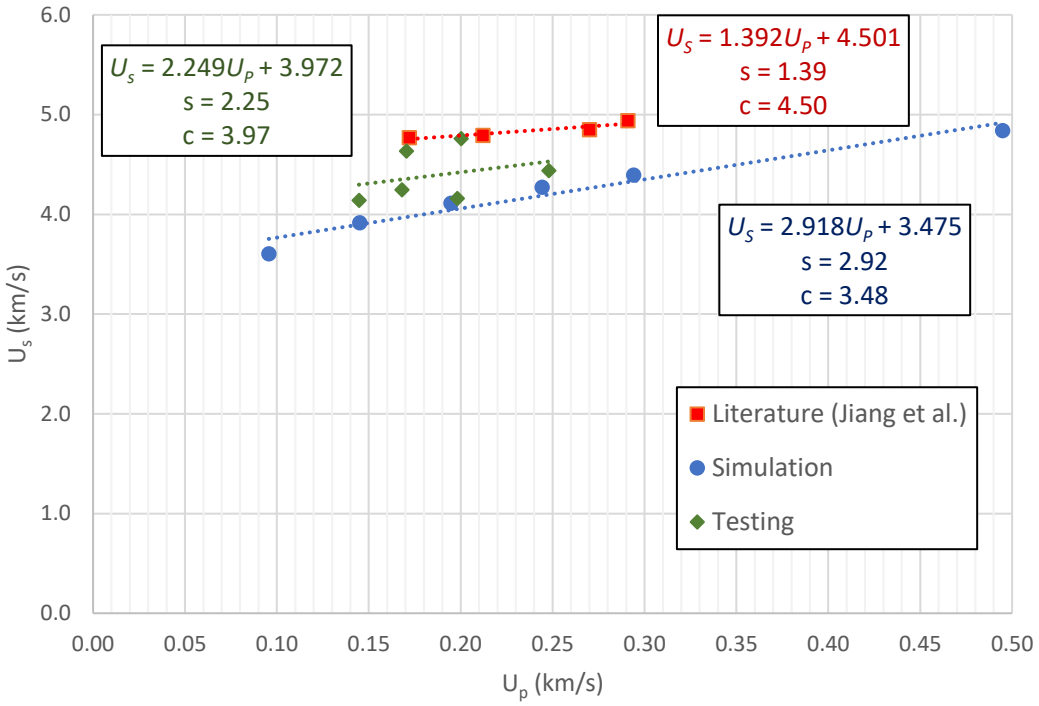

Figure 3.5. U_S–U_P relations found in experiment compared to MD Simulation and previous literature [9] which allows equation of state to be derived.

To begin, we are unable to determine the HEL of the material from these measurements. Calculations performed to determine the coefficients of the Hugoniot EOS relied upon published values. The PDV measurements are unable to provide a velocity-time profile from which this limit could be deduced as it is in other studies [12] requiring less-available gas-gun experimental setups. Second, while there are minor variations in these values between similar materials [12] and the impacts of these variations are minor for the purposes of this study, they do highlight a shortcoming of this experimental approach. A novel material with unknown values would have no clear counterparts to reference for a reasonable approximation of its elastic limit. Therefore, there would be little confidence in the results generated in these studies.

Additionally, there were greater variations in the PDV measurements of the present study than those found in previous studies using traditional DPS methods. This variation is presumed to be caused by several factors. First, the homodyne PDV system used had significant noise at lower frequencies. As a result of this, trials with velocity profiles below ~0.13 km/s did not provide useful results. On the other side of this envelope, the current experimental setup and procedures

are unable to achieve the high velocities necessary for testing over a large range. While it is known that thinner flyers will achieve higher impact velocities and generate greater shock velocities, there are limitations to reducing thickness. Polishing below 10 μm creates uneven shapes and surfaces of the flyer non-conducive for testing. Furthermore, the impacts with these thinner flyers do not create strong shock signals for determining the particle velocity in the LiF target.

To mitigate these issues, several modifications are proposed for future work. Improvements to the current system can allow for greater determination of impact and particle velocities behind the shock, especially those occurring at lower velocities. Several authors have proposed an implementation of a heterodyne PDV system in flyer-impact experiments [30–32] rather than the current homodyne system used for this study. Referring to Figure 2, instead of splitting the 1550 nm CW laser prior to mixing with the returned signal, another signal with a wavelength of 0.1 pm difference is mixed. This allows for the noise which typically occurs around the 0–0.1 GHz band to upshift to >1.5 GHz, well out-side of the testing range. This upshift allows for further testing of the lower velocities. To achieve higher velocities, an increase in power in laser energy beyond 0.8 J over the same pulse width can achieve higher impact velocities for same-thickness flyers. Laser power cannot be increased continually without potentially damaging the flyer during launch; however, small increases could allow for testing over an increased range of velocities, allowing for greater fidelity in conclusions regarding the Hugoniot coefficients.

3.4.2 Spall Strength

Figure 2.6a shows a PDV measurement during the impact experiments of HEA target using aluminum flyers. These experiments provide a direct measurement of the free surface velocity of the HEA alloy samples during impact with the aluminum flyer. This velocity profile is the signature of a spall failure where material begins to lose cohesive strength under dynamic tension and pieces of the target material begin to separate from the overall foil. Figure 2.6b shows how this failure appears within the HEA targets after testing. The tensile wave interactions resulting from reflections of the shock wave have exceeded the local tensile strength of the HEA sample. These failures result in the nucleation of voids within the material. A spall failure along the surface of the sample is readily apparent where a crack has propagated due to material separation.

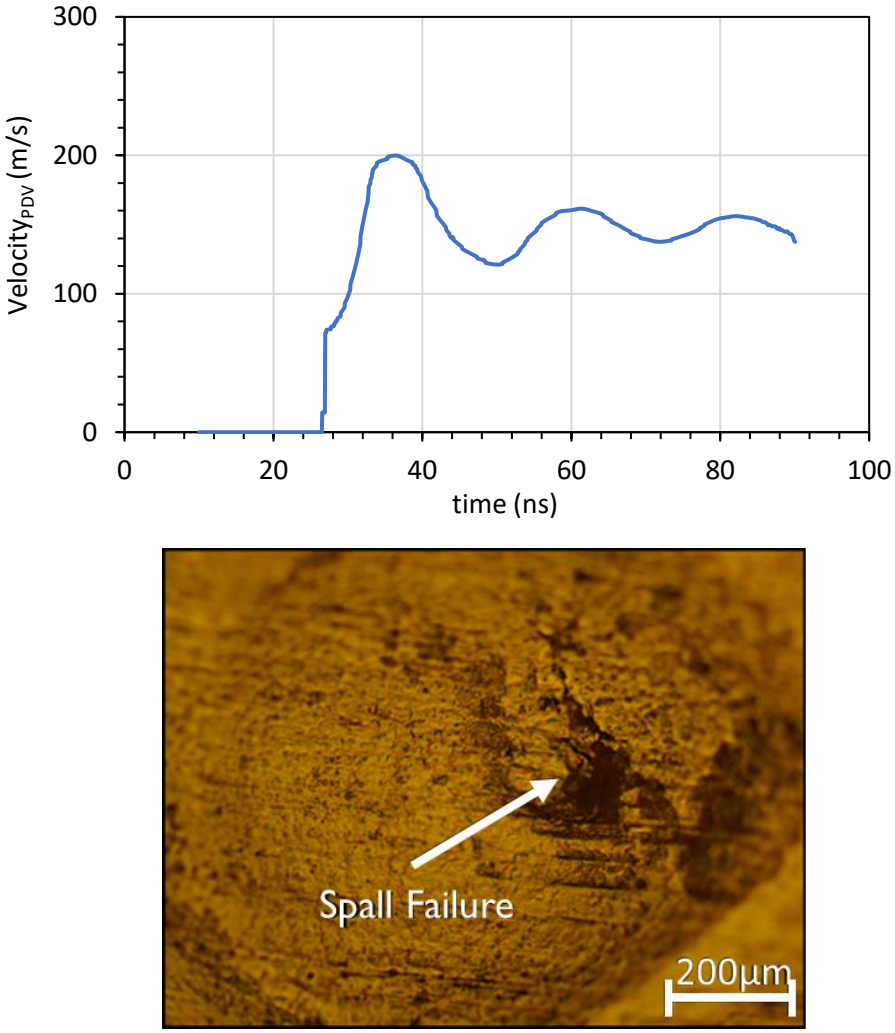

Figure 3.6. (a) Particle velocity measured from the free surface of the HEA target (b) Spall failure in the target.

The free surface velocity history shown in Figure 2.6a can be analyzed to understand the stress history in the target throughout the spall failure process. At ~39 ns, the free surface velocity peaks at around 200 m/s. This peak free surface velocity corresponds to the maximum compressive hydrostatic stress seen in the sample. The free surface velocity measured by the PDV then decreases until reaching a local minimum. This ″pullback″ velocity signal occurs at ~50 ns, while the free surface velocity is 121 m/s. The corresponding "pullback" velocity defined as Δv, is measured as ~79 m/s in this trial. From here, the spall strength of the material is then estimated using Equation (3). The strain rate induced by the flyer impacts within the HEA samples are also

determined. Strain rate is determined based upon the slope of the velocity profile at the midpoint between the peak compressive stress and the pullback signal.

This strain rate will differ depending on the thickness of the aluminum flyer used in the trial. Aluminum flyers of 25 µm and 50 µm thicknesses were used in these experiments which had resulting flyout velocities prior to impact with the HEA targets of around 1.0 km/s and 0.5 km/s, respectively. The differences in these flyouts and the resulting impacts produced different free surface velocity profiles. The variations of the spall strength and the strain rate for each test scenario are shown in Figure 2.7.

In Figure 2.7, the data point corresponding to the 50 µm aluminum flyers had a strain rate of 1.58 μs^{-1} with an observed spall strength of 1.64 GPa. Meanwhile, for the 25 µm flyer case, where the impact velocity was nearly double that of the 50 µm, the strain rate was 6.02 μs^{-1}, with a spall strength of 3.00 GPa. The higher velocity impacts resulted in both a higher strain rate and greater spall strength being observed within the HEA samples. This positive correlation between these two variables is expected. Previous studies on similar materials observed similar behaviors [10,11].

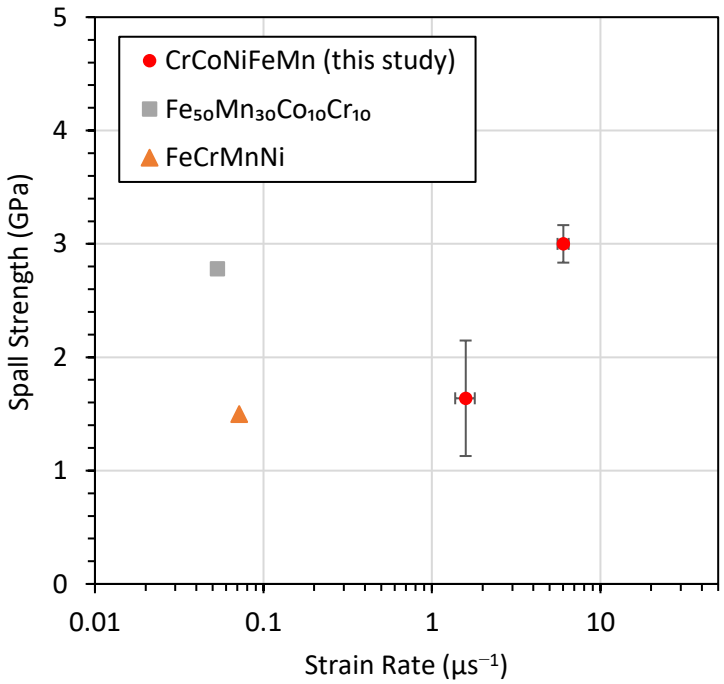

Figure 3.7. Strain rate dependence of spall strength for CoCrFeMnNi alloy compared to similar alloys.

Figure 2.7 also shows a comparison of the CoCrFeMnNi HEA sample tested in this study to previous spall–strain rate studies examining similar HEAs produced under conventional methods [10,11]. These studies tested at strain rate magnitudes lower than those present in these experiments. However, the spall strengths of those materials at those lower strain rates are similar to the spall strength determined for this HEA produced using AM methods. There can be several reasons for these discrepancies. Analysis of the specimens impacted by 25 μm flyers did not show the evident spall failures of those impacted by the 50 μm flyers seen in Figure 2.6b. It is possible that the tensile stress waves created by these failures were insufficient to produce a strong spall failure. Thus, the spall strength observed in these higher strain rate tests may not fully reflect the behavior of the material. In future studies, achieving higher strain rates with flyers in excess of 50 μm thickness would be desired. These trials have shown that spallation occurs throughout the sample, increasing confidence that the spall strength calculated accurately reflects the material's behavior. To achieve higher strain rates with these flyers would require certain modifications to the current experimental design. Increasing the energy of the laser at the point of launch can best increase the impact velocity of the aluminum flyers. Similar to the solutions addressed in the previous section, increasing the energy output of a single pulse at the point of launch through the use of a different pulse laser or modifications to the diffractive elements prior to the aspheric lens in order to decrease spot size would achieve this. Flyers of 50 μm and greater could then be used to achieve the high strain rates produced by the 25 μm flyers in these studies while still producing evident spall failures.

Additionally, differences between the AM CoCrFeMnNi samples tested in this study and the compared HEA specimens may have resulted in similar spall strengths despite the increased strain rates present. While the compositions of these materials differ and could have contributed to these discrepancies, there are also dissimilarities in the manufacturing processes. These differing processes may have resulted in microstructural features that can better explain these findings. To do so, post-shock recovered samples were examined to identify and characterize the spall failures in the samples.

3.4.3 Fractography Analysis

High-magnification images were taken using an SEM of the post-shock recovered samples in order to better observe the spallation within the material. In Figure 2.8, a cross-section of a post-

impacted 100 µm HEA target with the aluminum flyer plate is shown. Outlined in Figure 2.8 is the region highlighted by the black box in which spall is expected to occur based upon calculations involving wave speed and thicknesses of the target and flyer [29]. The other red-highlighted regions indicate the regions in which spallation damage was observed within the sample. The enlarged images of these areas show rounded crack tips. This indicates ductile behavior in the HEA sample despite the high strain rates present.

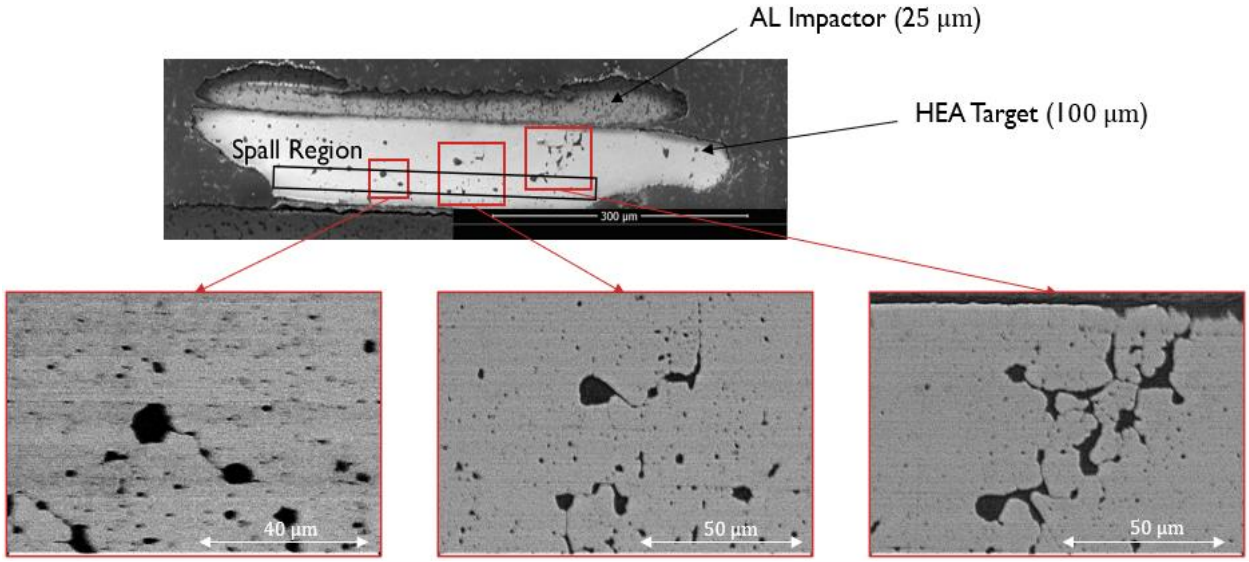

Figure 3.8. Post-impact cross-section images showing spallation in HEA target both within and outside of predicted spall region.

Also notable in these analyses are the locations at which spall failure occurred. While spallation is observed within the expected region, as shown in the left and center enlarged images of Figure 2.8, there are also indications of spall failure outside of these regions, as shown in the right image. These failures occurred much nearer to the surface, between the HEA target and the aluminum impactor. While these failures appear to be of a similar nature as those in the expected spall region as indicated by the rounded crack tips indicative of ductile failure, the formation of these failures in an unanticipated location is investigated.

To understand the presence of these spall failures outside of the predicted spall planes, we acquired further SEM images to reveal features in the microstructure of this material, prior to impact experiments. In Figure 2.9, the two images in the top left show the presence of both pores and low atomic number (Z) constituents throughout the samples. The low atomic number constituents are distinguishable from the porosities in the secondary electron SEM image in Figure

2.9b, which shows topographic features. The corresponding EDS maps show local enrichment of Cr and O in the areas corresponding to the low-Z constituents, suggesting that these are Cr-oxides. However, these cannot be identified as oxides with complete certainty because the O Kα X-ray line at 0.525 keV is unable to be deconvoluted from the Cr Lα line at 0.573 eV on the EDS elemental spectrum. Due to the overlapping X-ray energies, further characterization of these AM samples would be needed to confirm that the light elemental phases shown in the EDS elemental maps are indeed Cr-oxides. It is hypothesized that during the laser-based DED AM process, chromium preferentially oxidized to form these chromium-oxide deposits in the material. Regardless, both the formation of these low-Z constituents as well as the porosities observed in the material may have served as nucleation sites about which the crack could propagate when subjected to the tensile waves induced by the shock [33]. The presence of these areas outside of the predicted spall plane thus resulted in crack formation as observed in the spall failure samples. To understand which of these two features is responsible for the failures, or whether both equally contributed, further EDS imagining of post-impact samples would be required.

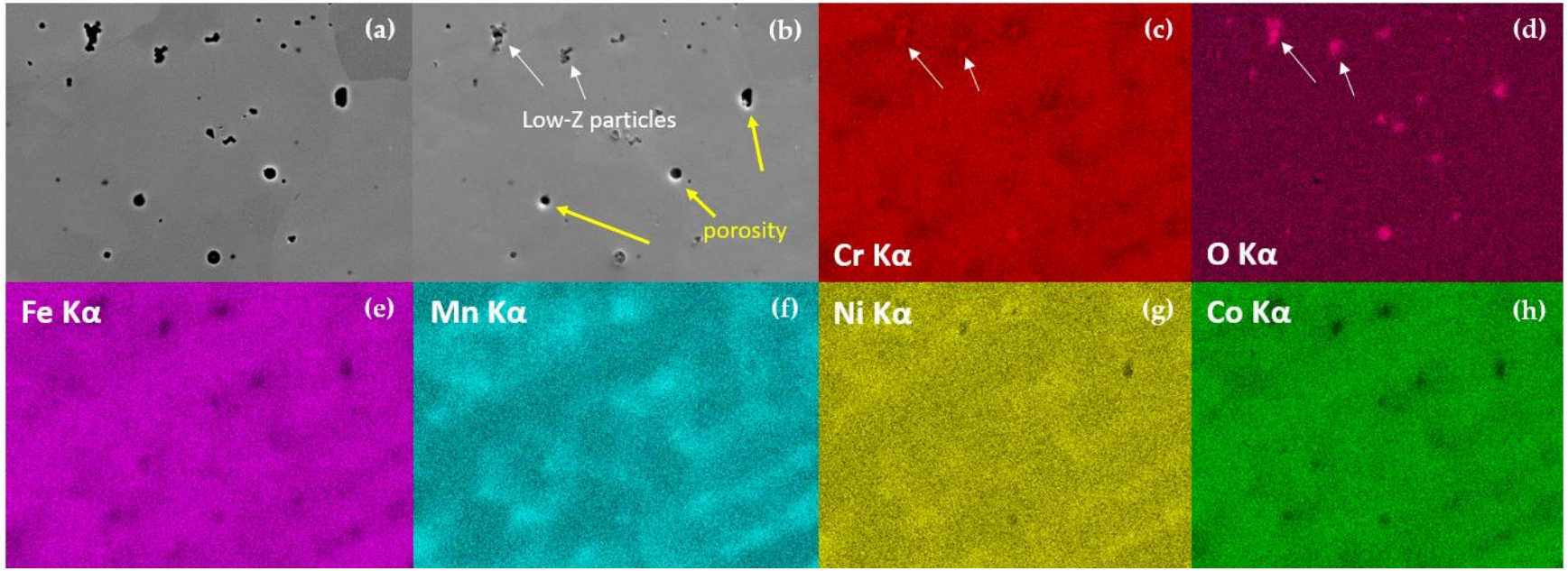

`Figure 3.9. Backscatter SEM (a) and secondary electron SEM (b) images of porosities and low atomic number constituents within HEA sample with the corresponding EDS elemental maps (c–h). Windows 50 µm wide at 20 kV.

3.5 Conclusions

In this study, we investigated the behavior of an AM CoCrFeMnNi HEA when subjected to shock loading via an LIPIT system. This approach allows for greater versatility in studying the dynamic behaviors of novel materials compared to traditional methods involving DPS and gas-gun experiments.

- Determination of Hugoniot EOS coefficient and bulk sound speed can be determined from PDV measurements. These results are reliant upon HEL data from similar materials to be available.
- Future EOS determination can be improved through testing across a wider range of impact velocities and the implementation of an improved heterodyne PDV system compared to the available homodyne system used in this study.
- Spall strength determination using the free surface velocity of the HEA targets showed measured spall strength approximately increased material spall strength at higher strain rates.
- Achieving higher impact velocities with flyers of at least 50 μm thickness will produce greater spallation in the materials and lend greater confidence in the accurate assessment of the material's spall strength.
- Post-shock recovered samples showed evidence of ductile fracture in spall regions. This spallation occurred both within and outside of the region predicted by the shock wave speeds.
- SEM imaging showed the presence of voids in areas outside of the predicted spall region. Furthermore, EDS elemental maps showed the presence of Cr-rich oxides as well as porosities within the HEA samples.
- Porosities and Cr-oxides outside of the predicted spall region may have served as void nucleation sites, explaining spallation observed throughout post-impacted samples rather than analytically predicted regions.
- Further investigation into the exact microstructural features in the failure regions will better describe whether the voids' formations are more attributable to the pores or low-Z constituents.

- Refinement of the manufacturing process to prevent the formation of the porosities and low-Z constituents may allow for increased spall strength in the material at high strain rates.

3.6 Author Contributions

Conceptualization, A.D.; methodology, A.D. and A.E.; software, A.D.; validation, A.D. and A.E.; formal analysis, A.D. and A.E.; investigation, A.D., A.E., E.B., and A.K.; resources, E.B., R.D., and A.K.; data curation, A.E.; writing—original draft preparation, A.D. and A.E.; writing—review and editing, A.E., T.D., R.D., A.K., E.B., and V.T.; visualization, A.D., A.E., E.B., and A.K.; supervision, V.T.; project administration, V.T.; funding acquisition, R.D. and V.T. All authors have read and agreed to the published version of the manuscript.

3.7 Acknowledgements

Funding: This research was funded by Sandia National Laboratories, grant number 2193858.

Acknowledgments: R.D. is supported by the Center for Integrated Nanotechnologies, an Office of Science User Facility operated for the U.S. Department of Energy. Sandia National Laboratories is a multi-mission laboratory managed and operated by National Technology and Engineering Solutions of Sandia, LLC., a wholly owned subsidiary of Honeywell International, Inc., for the U.S. Department of Energy's National Nuclear Security Administration under contract DE-NA0003525. The views expressed in this article do not necessarily represent the views of the U.S. Department of Energy or the United States Government.

Conflicts of Interest: The authors declare no conflict of interest.

3.8 References

[1] Dada, M.; Popoola, P.; Adeosun, S.; Mathe, N. High Entropy Alloys for Aerospace Applications. Aerodynamics 2021, 7, 1–16. https://doi.org/10.5772/intechopen.84982.

[2] Dixit, S.; Rodriguez, S.; Jones, M.R.; Buzby, P.; Dixit, R.; Argibay, N.; DelRio, F.W.; Lim, H.H.; Fleming, D. Refractory High-Entropy Alloy Coatings for High-Temperature Aerospace and Energy Applications. J. Therm. Spray Technol. 2022, 31, 1021–1031. https://doi.org/10.1007/s11666-022-01324-0.

[3] Ye, Y.; Wang, Q.; Lu, J.; Liu, C.; Yang, Y. High-entropy alloy: Challenges and prospects. Mater. Today 2015, 19, 349–362. https://doi.org/10.1016/j.mattod.2015.11.026.

[4] Cantor, B.; Chang, I.T.H.; Knight, P.; Vincent, A.J.B. Microstructural development in equiatomic multicomponent alloys. Mater. Sci. Eng. A 2004, 375–377, 213–218. https://doi.org/10.1016/j.msea.2003.10.257.

[5] Yeh, J.-W.; Chen, S.K.; Lin, S.-J.; Gan, J.-Y.; Chin, T.-S.; Shun, T.-T.; Tsau, C.-H.; Chang, S.-Y. Nanostructured High-Entropy Alloys with Multiple Principal Elements: Novel Alloy Design Concepts and Outcomes. Adv. Eng. Mater. 2004, 6, 299–303. https://doi.org/10.1002/adem.200300567.

[6] Miracle, D.B.; Senkov, O.N. A critical review of high entropy alloys and related concepts. Acta Mater. 2017, 122, 448–511. https://doi.org/10.1016/j.actamat.2016.08.081.

[7] Gali, A.; George, E. Tensile properties of high- and medium-entropy alloys. Intermetallics 2013, 39, 74–78. https://doi.org/10.1016/j.intermet.2013.03.018.

[8] Gludovatz, B.; Hohenwarter, A.; Catoor, D.; Chang, E.H.; George, E.P.; Ritchie, R.O. A fracture-resistant high-entropy alloy for cryogenic applications. Science 2014, 345, 1153–1158. https://doi.org/10.1126/science.1254581.

[9] Zhang, Z.; Mao, M.M.; Wang, J.; Gludovatz, B.; Zhang, Z.; Mao, S.X.; George, E.; Yu, Q.; Ritchie, R.O. Nanoscale origins of the damage tolerance of the high-entropy alloy CrMnFeCoNi. Nat. Commun. 2015, 6, 10143. https://doi.org/10.1038/ncomms10143.

[10] Yang, Y.; Yang, S.; Wang, H. Effects of microstructure on the evolution of dynamic damage of Fe50Mn30Co10Cr10 high en-tropy alloy. Mater. Sci. Eng. A 2020, 802, 140440. https://doi.org/10.1016/j.msea.2020.140440.

[11] Hawkins, M.C.; Thomas, S.A.; Hixon, R.S.; Gigax, J.; Li, N.; Fensin, S. Dynamic Properties of FeCrMnNi, a High Entropy Alloy; Nevada National Security Site (NNSS): North Las Vegas, NV, USA, 2021.

[12] Jiang, Z.J.; He, J.Y.; Wang, H.Y.; Zhang, H.S.; Lu, Z.P.; Dai, L.H. Shock compression response of high entropy alloys. Mater. Res. Lett. 2016, 4, 226–232. https://doi.org/10.1080/21663831.2016.1191554.

[13] Peralta, P.; Digiacomo, S.; Hashemian, S.; Luo, S.-N.; Paisley, D.; Dickerson, R.; Loomis, E.; Byler, D.; McClellan, K.; D'Armas, H. Characterization of Incipient Spall Damage in Shocked Copper Multicrystals. Int. J. Damage Mech. 2008, 18, 393–413. https://doi.org/10.1177/1056789508097550.

[14] Fujiwara, H.; Brown, K.E.; Dlott, D.D. High-energy flat-top beams for laser launching using a Gaussian mirror.. Appl. Opt. 2010, 49, 3723–3731. https://doi.org/10.1364/ao.49.003723.

[15] Brown, K.E.; Shaw, W.L.; Zheng, X.; Dlott, D. Simplified laser-driven flyer plates for shock compression science. Rev. Sci. Instruments 2012, 83, 103901. https://doi.org/10.1063/1.4754717.

[16] Curtis, A.D.; Banishev, A.A.; Shaw, W.L.; Dlott, D.D. Laser-driven flyer plates for shock compression science: Launch and target impact probed by photon Doppler velocimetry. Rev. Sci. Instruments 2014, 85, 043908. https://doi.org/10.1063/1.4871361.

[17] Mallick, D.; Zhao, M.; Parker, J.; Kannan, V.; Bosworth, B.; Sagapuram, D.; Foster, M.; Ramesh, K. Laser-driven flyers and nanosecond-resolved velocimetry for spall studies in thin metal foils. Exp. Mech. 2019, 59, 611–628.

[18] Mallick, D.D.; Ramesh, K. Dynamic fragmentation of boron carbide using laser-driven flyers. Int. J. Impact Eng. 2019, 136, 103416. https://doi.org/10.1016/j.ijimpeng.2019.103416.

[19] Luo, S.N.; Swift, D.C.; Tierney, T.E.; Paisley, D.L.; Kyrala, G.A.; Johnson, R.P.; Hauer, A.A.; Tschauner, O.; Asimow, P.D. La-ser-induced shock waves in condensed matter: Some techniques and applications. High Press. Res. 2004, 24, 409–422. https://doi.org/10.1080/08957950412331331709.

[20] Swift, D.C.; Niemczura, J.G.; Paisley, D.L.; Johnson, R.P.; Luo, S.-N.; Iv, T.E.T. Laser-launched flyer plates for shock physics experiments. Rev. Sci. Instrum. 2005, 76, 093907. https://doi.org/10.1063/1.2052593.

[21] Shui, M.; Chu, G.; Zhu, B.; He, W.; Xi, T.; Fan, W.; Xin, J.; Gu, Y. Hypervelocity launching of flyers at the SG-III prototype laser facility. J. Appl. Phys. 2016, 119, 035903. https://doi.org/10.1063/1.4940244.

[22] Zhu, Y.; Liao, X.; Wu, X. Deformation twinning in nanocrystalline materials. Prog. Mater. Sci. 2012, 57, 1–62. https://doi.org/10.1016/j.pmatsci.2011.05.001.

[23] Thürmer, D.; Zhao, S.; Deluigi, O.R.; Stan, C.; Alhafez, I.A.; Urbassek, H.M.; Meyers, M.A.; Bringa, E.M.; Gunkelmann, N. Exceptionally high spallation strength for a high-entropy alloy demonstrated by experiments and simulations. J. Alloy. Compd. 2021, 895, 162567. https://doi.org/10.1016/j.jallcom.2021.162567.

[24] Melia, M.A.; Carroll, J.D.; Whetten, S.R.; Esmaeely, S.N.; Locke, J.; White, E.; Anderson, I.; Chandross, M.; Michael, J.R.; Argibay, N.; et al. Mechanical and Corrosion Properties of Additively Manufactured CoCrFeMnNi High Entropy Alloy. Addit. Manuf. 2019, 29. https://doi.org/10.1016/j.addma.2019.100833.

[25] Dhiman, A.; Olokun, A.; Tomar, V. Microscale Analysis of Stress Wave Propagation through Plastic Bonded Explosives un-der Micro-Sphere Shock Impact. J. Dyn. Behav. Mater. 2021, 7, 294–306.

[26] Dhiman, A.; Rai, A.; Wang, H.; Prakash, C.; Tomar, V. Dynamic Stress Evaluation due to Hypervelocity Impact using Time Gated Raman Spectroscopy. DYMAT Winter Sch. 2020, 12, 1–6.

[27] Marsh, S.P. LASL Shock Hugoniot Data; University of California press: Berkeley, CA, USA, 1980.

[28] Meyers, M.A. Dynamic Behavior of Materials; John Wiley & Sons: New York, NY, USA, 1994.

[29] Thomas, S.; Hawkins, M.; Matthes, M.; Gray III, G.; Hixson, R. Dynamic strength properties and alpha-phase shock Hugoniot of iron and steel. J. Appl. Phys. 2018, 123, 175902.

[30] Holtkamp, D.B. Survey of Optical Velocimetry Experiments Applications of PDV, A Heterodyne Velocimeter. In proceed-ings of the 2006 IEEE International Conference on Megagauss Magnetic Field Generation and Related Topics, Santa Fe, NM, USA, 5–10 November 2006; pp. 119–128. https://doi.org/10.1109/megaguss.2006.4530668.

[31] Kettenbeil, C.; Mello, M.; Bischann, M.; Ravichandran, G. Heterodyne transverse velocimetry for pressure-shear plate impact experiments. J. Appl. Phys. 2018, 123, 125902. https://doi.org/10.1063/1.5023007.

[32] Mallick, D.; Zhao, M.; Bosworth, B.; Schuster, B.; Foster, M.; Ramesh, K. A Simple Dual-Beam Time-Multiplexed Photon Doppler Velocimeter for Pressure-Shear Plate Impact Experiments. Exp. Mech. 2018, 59, 41–49. https://doi.org/10.1007/s11340-018-0435-y.

[33] Wayne, L.; Krishnan, K.; DiGiacomo, S.; Kovvali, N.; Peralta, P.; Luo, S.; Greenfield, S.; Byler, D.; Paisley, D.; McClellan, K. Statistics of weak grain boundaries for spall damage in polycrystalline copper. Scr. Mater. 2010, 63, 1065–1068. https://doi.org/10.1016/j.scriptamat.2010.08.003.

4. CONCLUSION

This work investigated the spall behavior of an AM CoCrFeMnNi HEA specimen when subjected to high-strain rate loading. A novel experimental setup using a high-energy pulse laser with a homodyne PDV system was used to record velocity profiles during high-speed impacts of thin disk flyers. This setup demonstrated the ability of this system to measure not only the spall strength and failure mechanisms of these materials, but also determine key shock parameters necessary for these spall strength calculations. This system is then capable of providing key measurements which were previously only possible using more expensive and less available gas-gun setups. Thus, key supplemental data and verification of numerical simulations are more readily accessible to address the ever-growing need for high-speed testing as the aerospace domain evolves.

The results of testing of the AM CoCrFeMnNi HEA showed that the Hugoniot parameters governing the propagation of shock in the material were like those found in traditionally manufactured samples and those predicted using MD simulations. Spall strength measurements determined that the AM specimens possessed equivalent strengths to similar HEAs although at significantly higher strain-rates. The higher-strain rates associated with these spall strengths and the occurrence of failures outside of the predicted spall region suggested the presence of microstructural features in the AM samples different from those of traditionally casted Cantor alloys. SEM-EDS imaging of the samples revealed likely chromium-oxide deposits and porosities throughout the sample that would not otherwise be present. These regions likely explain the differences in spall strengths as well as the occurrence of materials throughout the specimens instead of being limited to the predicted spall region. Eliminating the occurrence of these defects by manipulating AM production parameters could improve the performance of AM CoCrFeMnNi HEA specimens to be equivalent to traditionally manufactured Cantor alloys during high-strain loadings.

Three recommendations are made for future research building upon this work. First, the implementation of a heterodyne PDV system rather than the current homodyne version can expand the velocity range during testing to include lower velocities. This can build greater fidelity in these values to verify numerical simulations. Second is the incorporation of a higher energy pulse laser to achieve greater flyer velocities prior to impact. This would allow for testing to better determine

the effects of increasing strain-rates on the specimens as well as the creation of clearer spall regions to better analyze the failure mechanisms. Finally, EDS mapping of post-shock samples may be able to determine the exact microstructural defects responsible for the differing behavior of AM samples during high-velocity impacts. Doing so would allow for more precision in refining the AM process.

REFERENCES

Literature Review

[1] Britannica, T. Editors of Encyclopaedia (2021, March 27). alloy. Encyclopedia Britannica. ` https://www.britannica.com/technology/alloy

[2] Yeh, J.-W.; Chen, S.K.; Lin, S.-J.; Gan, J.-Y.; Chin, T.-S.; Shun, T.-T.; Tsau, C.-H.; Chang, S.-Y. Nanostructured High-Entropy Alloys with Multiple Principal Elements: Novel Alloy Design Concepts and Outcomes. Adv. Eng. Mater. 2004, 6, 299–303. https://doi.org/10.1002/adem.200300567.

[3] Cantor, B.; Chang, I.T.H.; Knight, P.; Vincent, A.J.B. Microstructural development in equiatomic multicomponent alloys. Mater. Sci. Eng. A 2004, 375–377, 213–218. https://doi.org/10.1016/j.msea.2003.10.257.

[4] Zhang, Z.; Mao, M.M.; Wang, J.; Gludovatz, B.; Zhang, Z.; Mao, S.X.; George, E.; Yu, Q.; Ritchie, R.O. Nanoscale origins of the damage tolerance of the high-entropy alloy CrMnFeCoNi. Nat. Commun. 2015, 6, 10143. https://doi.org/10.1038/ncomms10143.

[5] Gludovatz, B.; Hohenwarter, A.; Catoor, D.; Chang, E.H.; George, E.P.; Ritchie, R.O. A fracture-resistant high-entropy alloy for cryogenic applications. Science 2014, 345, 1153–1158. https://doi.org/10.1126/science.1254581.

[6] J.Y. He, W.H. Liu, H. Wang, Y. Wu, X.J. Liu, T.G. Nieh, Z.P. Lu. Effects of Al addition on structural evolution and tensile properties of the FeCoNiCrMn high-entropy alloy system. Acta Materialia. 2014, 62, 105-113. https://doi.org/10.1016/j.actamat.2013.09.037.

[7] 6 - Production and casting of aerospace metals. (2012). In A. P. Mouritz (Ed.), Introduction to Aerospace Materials (pp. 128-153). Woodhead Publishing. https://doi.org/https://doi.org/10.1533/9780857095152.128.

[8] Herzog, D., Seyda, V., Wycisk, E., & Emmelmann, C. (2016). Additive manufacturing of metals. Acta Materialia, 117, 371-392. https://doi.org/https://doi.org/10.1016/j.actamat.2016.07.019

[9] Piglione, A., Dovgyy, B., Liu, C., Gourlay, C. M., Hooper, P. A., & Pham, M. S. (2018). Printability and microstructure of the CoCrFeMnNi high-entropy alloy fabricated by laser powder bed fusion. Materials Letters, 224, 22-25. https://doi.org/https://doi.org/10.1016/j.matlet.2018.04.052

[10] Li, R., Niu, P., Yuan, T., Cao, P., Chen, C., & Zhou, K. (2018). Selective laser melting of an equiatomic CoCrFeMnNi high-entropy alloy: Processability, non-equilibrium microstructure and mechanical property. Journal of Alloys and Compounds, 746, 125-134. https://doi.org/https://doi.org/10.1016/j.jallcom.2018.02.298

[11] Kustas, A. B., Susan, D. F., Johnson, K. L., Whetten, S. R., Rodriguez, M. A., Dagel, D. J., & Argibay, N. (2018). Characterization of the Fe-Co-1.5V soft ferromagnetic alloy processed by Laser Engineered Net Shaping (LENS). Additive Manufacturing, 21, 41-52. https://doi.org/https://doi.org/10.1016/j.addma.2018.02.006

[12] Melia, M.A.; Carroll, J.D.; Whetten, S.R.; Esmaeely, S.N.; Locke, J.; White, E.; Anderson, I.; Chandross, M.; Michael, J.R.; Argibay, N.; et al. Mechanical and Corrosion Properties of Additively Manufactured CoCrFeMnNi High Entropy Alloy. Additive Manufacturing 2019, 29. https://doi.org/10.1016/j.addma.2019.100833.

[13] Meyers, M.A. Dynamic Behavior of Materials; John Wiley & Sons: New York, NY, USA, 1994.

[14] Antoun, T.; Curran, D. R.; Razorenov, S.V.; Seaman, L.; Kanel, G. I.; & Utkin, A. V. Spall Fracture. Springer Science + Business: New York, NY, USA. 2003. https://doi.org/10.1007/b97226

[15] Jiang, Z.J.; He, J.Y.; Wang, H.Y.; Zhang, H.S.; Lu, Z.P.; & Dai, L.H. Shock compression response of high entropy alloys. Mater. Res. Lett. 2016, 4, 226–232. https://doi.org/10.1080/21663831.2016.1191554.

[16] Ahrens, T.J.; Gust W.H.; & Royce E.B. Material strength effect in the shock compression of alumina. Journal of Applied Physics, 39, 4610. https://doi.org/10.1063/1.1655810

[17] Xi, F.; Yu, Y.; Dai, C.; et al. Shock compression response of a Zr-based bulk metallic glass up to 110 GPa. Journal of Applied Physics, 38, 2689-2696. https://doi.org/10.1063/1.3501044

[18] Luo, S.N.; Swift, D.C.; Tierney, T.E.; Paisley, D.L.; Kyrala, G.A.; Johnson, R.P.; Hauer, A.A.; Tschauner, O.; & Asimow, P.D. Laser-induced shock waves in condensed matter: Some techniques and applications. High Press. Res. 2004, 24, 409–422. https://doi.org/10.1080/08957950412331331709.

[19] Swift, D.C.; Niemczura, J.G.; Paisley, D.L.; Johnson, R.P.; Luo, S.-N.; & Iv, T.E.T. Laser-launched flyer plates for shock physics experiments. Rev. Sci. Instrum. 2005, 76, 093907. https://doi.org/10.1063/1.2052593.

[20] Marsh, S.P. LASL Shock Hugoniot Data; University of California press: Berkeley, CA, USA, 1980.

[21] Strand, O. T.; Goosman, D. R.; Martinez, C.; & Whitworth, T.L. "Velocimetry using heterodyne techniques," 26th Int. Conf. on High-speed Photography and Photonics, Alexandria, VA September 19-24, 2004, Proc. of SPIE 5580 (2005) 593. https://doi.org/10.1063/1.2336749

[22] D. B. Holtkamp, "Survey of Optical Velocimetry Experiments - Applications of PDV, A Heterodyne Velocimeter," 2006 IEEE International Conference on Megagauss Magnetic Field Generation and Related Topics, 2006, pp. 119-128, https://doi.org/10.1109/MEGAGUSS.2006.4530668.

[23] Mallick, D.; Zhao, M.; Parker, J.; Kannan, V.; Bosworth, B.; Sagapuram, D.; Foster, M.; & Ramesh, K. Laser-driven flyers and nanosecond-resolved velocimetry for spall studies in thin metal foils. Exp. Mech. 2019, 59, 611–628. https://doi.org/10.1007/s11340-019-00519-x

Article Citation

Ehler, A., Dhiman, A., Dillard, T., Dingreville, R., Barrick, E., Kustas, A., & Tomar, V. (2022). High-Strain Rate Spall Strength Measurement for CoCrFeMnNi High-Entropy Alloy. Metals, 12(9). https://doi.org/10.3390/met12091482